ARTICLES

PEGylated carbon dot/MnO$_2$ nanohybrid: a new pH/H$_2$O$_2$-driven, turn-on cancer nanotheranostics

Shiqing Chen[1,2], Qingyan Jia[1,2], Xiuli Zheng[1,2], Yongmei Wen[1,2], Weimin Liu[1,2], Hongyan Zhang[1,2], Jiechao Ge[1,2*] and Pengfei Wang[1,2]

ABSTRACT   The effect of tumor-targeted photodynamic therapy (PDT) was improved by designing nanotheranostics to promote oxygenation in a tumor microenvironment (TME) wherein hypoxia, acidosis, and the elevated levels of H$_2$O$_2$ are three main characteristics. In this study, a carbon dot (CD) PDT agent recently developed by our group was firstly applied as reducing agent to react with potassium permanganate for fabricating CDs/manganese dioxide (CDs/MnO$_2$) composites, which were in turn modified with polyethylene glycol (PEG) to form water-soluble CDs/MnO$_2$-PEG nanohybrids. In a normal physiological environment, the as-prepared nanohybrids exhibited quenched fluorescence, weak singlet oxygen generation, and low magnetic resonance imaging (MRI) signal. However, given the high sensitivity of MnO$_2$ to the TME, the CDs/MnO$_2$-PEG nanohybrids changed from an "off" to an "on" state with synchronously enhanced fluorescence, singlet oxygen generation, and MRI signal in the TME. In vitro and in vivo analyses have revealed that CDs/MnO$_2$-PEG nanohybrids could be applied as TME-driven, turn-on nanotheranostics for the MR/fluorescence bimodal imaging-guided PDT of cancer. Moreover, complete clearance of CDs/MnO$_2$-PEG nanohybrids from the body of mice was observed, indicating their low long-term toxicity and good biocompatibility. This work offers a new nanotheranostic candidate for modulating the unfavorable TME, particularly for the targeted PDT of cancer through precise positioning and oxygen generation.

Keywords: tumor microenvironment, photodynamic therapy, carbon dots, turn-on theranostics, manganese dioxide

INTRODUCTION

Nanotheranostics that combine medical diagnostics and therapeutics into one nanosystem have been considered as the key toward realizing personalized nanomedicine for the precise treatment of cancer in the future [1–7]. In the past decade, numerous studies have explored various multifunctional theranostics nanosystems based on external (e.g., ultrasound, light, magnetic and electrical fields) or internal factors (e.g., pH value, redox, environment, and enzyme) [8–21]. Among them, pH/H$_2$O$_2$-driven nanotheranostics have been proven capable of markedly improving the O$_2$-dependent photodynamic therapy (PDT) of hypoxic tumors, as revealed by the interesting results obtained in pre-clinical animal experiments. The reason is that pH/H$_2$O$_2$-driven nanotheranostics can produce great amounts of oxygen in situ and modify the pH via a redox reaction with the acidic H$_2$O$_2$ in the tumor microenvironment (TME) [22–26]. For example, the extensively investigated pH/H$_2$O$_2$-driven nanotheranostics are MnO$_2$ nanoparticles and MnO$_2$-containing nanocomposites, which can improve tumor oxygenation to enhance the efficiency of PDT in the TME [27]. In addition, these nanoparticles and nanocomposites can also be rapidly reduced to water-soluble Mn^{2+} for T1-weighted magnetic resonance imaging (MRI) [28]. Thus, the study of MnO$_2$-based nanotheranostics can offer insight into the development of next-generation intelligent stimuli-responsive nanomedicines for the efficient diagnosis and treatment of cancer in the future. However, MnO$_2$-based nanotheranostics fabricated by current synthetic methods are hindered by the following limitations: 1) the complex and tedious preparation procedure; and 2) the need for drugs or photosensitizers for loading on MnO$_2$ nanoparticles [29]. Therefore, a simple method must be established for the preparation of MnO$_2$-based nanotheranostics.

Carbon dots (CDs), a new type of biocompatible fluorescent carbon material, have gained considerable interest in recent years because of their advantageous

---

[1] Key Laboratory of Photochemical Conversion and Optoelectronic Materials and CityU-CAS Joint Laboratory of Functional Materials and Devices, Technical Institute of Physics and Chemistry, Chinese Academy of Sciences, Beijing 100190, China
[2] School of Future Technology, University of Chinese Academy of Sciences, Beijing 100049, China
* Corresponding author (email: jchge2010@mail.ipc.ac.cn)

properties, including tunable emission, non-blinking fluorescence (FL) property, high photostability, excellent water solubility, and favorable biocompatibility [30–32]. These characteristics make CDs suitable for various applications, such as imaging agents [33,34], biosensors [35,36], and metal-free catalysts [37–39]. Meanwhile, nanotheranostics based on CDs have been recently developed because of the easy modification of CDs with drugs [40–48]. Moreover, the light-induced singlet oxygen ($^1O_2$) or heat generation of CDs have been developed recently by our group for PDT or photothermal therapy (PTT) of cancer, indicating their intrinsic capability for nanotheranostics [49–51]. According to the previous report [52], CDs also can function as reducing agents; therefore, the development of CDs with intrinsic photodynamic or photothermal properties as the reducing agent for preparing pH/H_2O_2-driven, CDs-based nanohybrids may provide new nanotheranostics candidates for simultaneous imaging and therapy of cancer.

Our group recently developed a novel CD PDT agent with a high $^1O_2$ quantum yield exceeding 1.3, thus enabling it to act as a novel nanotheranostics for the FL imaging-guided PDT of cancer [49]. In this study, such a CD PDT agent was firstly utilized as the reducing agent to react with $KMnO_4$. The resulting products were then modified with PEG to form CDs/MnO_2-PEG nanohybrids. In a normal physiological environment (pH 7.4), the obtained CDs/MnO_2-PEG nanohybrids exhibited quenched fluorescence, weak $^1O_2$ generation, and low MRI signal. With the introduction of acidic H_2O_2 into the TME of solid tumors (pH 6.5–6.9), the quenched fluorescence of CDs was recovered/enhanced for diagnosis/monitoring by the decomposition of MnO_2. The simultaneously generated Mn^{2+} can then be utilized as a contrast agent for MRI. Moreover, the MnO_2-H_2O_2 redox reaction at a reduced pH generated massive O_2 *in situ*, thereby significantly promoting the PDT efficacy of CDs (Scheme 1). Furthermore, complete clearance of CDs/MnO_2-PEG from the body of mice was achieved, indicating the low long-term toxicity and good biocompatibility of the fabricated nanohybrids. These findings highlight the promising potential of CDs/MnO_2-PEG nanohybrids for modulating the unfavorable TME and enhancing the PDT response to cancer.

EXPERIMENTAL SECTION

Chemicals and materials
Potassium permanganate ($KMnO_4$) and hydrogen peroxide (H_2O_2, 30 wt.% solution) were purchased from J&K Che-

mical Co. Amino group terminated glycol (mPEG-NH_2, M_w=2,000) was acquired from YareBio. All analytical-grade chemicals were commercially available and used without further purification unless indicated otherwise.

Synthesis of CDs/MnO_2
The strongly oxidizing $KMnO_4$ was one-step reduced by CDs to MnO_2. Then, the positively charged CDs were loaded on the formed MnO_2 nanosheets to obtain CDs/MnO_2 complexes. In brief, we prepared CDs by subjecting polythiophene (PT2) to hydrothermal treatment following our procedure in our previous study [49]. Then, 50 mL of $KMnO_4$ solution (0.02 mg mL^{-1}) was dropwise added to the activated CDs and stirred at room temperature for 6 h. Untreated $KMnO_4$ and unbound CDs were removed by ultrafiltration at 18,000 rpm for 10 min and washed with water thrice. After ultrasonic dispersion was conducted for 5 min, the large particles of the CDs/MnO_2 complexes were removed by centrifugation (7,000 rpm) and filtering through 0.22 mm membranes. The loading of the CDs onto the MnO_2 nanosheets was verified by measuring the samples with a UV-vis spectrophotometer. The quenching effect of MnO_2 on the CDs was observed with a luminescence spectrometer.

Synthesis of CDs/MnO_2-PEG
To prepare CDs/MnO_2-PEG NPs, approximately 25 mL of mPEG-NH_2 aqueous solution (25 mg, 1 mg mL^{-1}) was added to the solution under ultrasonication and then stirred vigorously at room temperature for 12 h to guarantee an efficient PEGylation. The resulting CDs/MnO_2-PEG was purified by a three-day dialysis procedure using a dialysis bag (MWCO 5,000 Da) to remove the unreacted mPEG-NH_2.

CDs loading ratio
The UV-vis-NIR spectra of CDs in CDs/MnO_2 nanohybrids were obtained after the nanohybrids were dissolved at pH 6.5 for 6 h. The UV-vis peaks at 492 nm were used to determine the concentration of CDs in the CDs/MnO_2 samples after the absorbance contributed by MnO_2 nanoparticles was removed by dissolving the samples at pH 6.5. The loading efficiency ($\varnothing_{CDs}$) of CDs can be calculated by the equation: $\varnothing_{CDs}=(Abs_{CDs}/Abs_{CDs/MnO_2\text{-}PEG})\times 100\%$, where Abs_{CDs} is the absorbance of CDs, and $Abs_{CDs/MnO_2\text{-}PEG}$ is the absorbance of CDs/MnO_2-PEG with the same concentration.

Detection of singlet oxygen
The CDs/MnO_2-PEG samples were loaded in a quartz
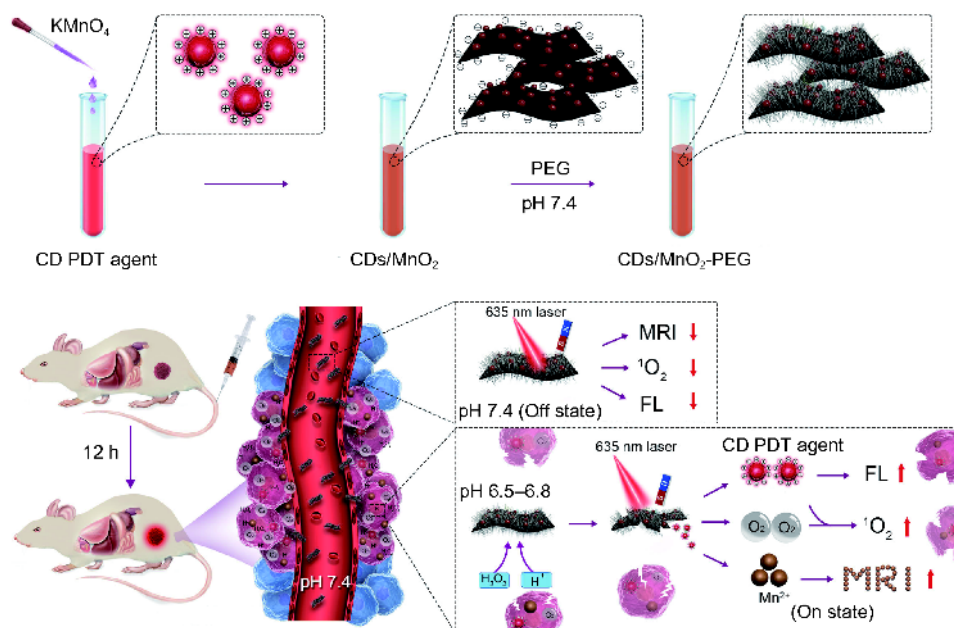
Scheme 1 Schematic illustration of CDs/MnO$_2$-PEG nanohybrids as a multimodal theranostics for the MR/FL imaging-guided PDT.

cuvette and exposed to laser at 635 nm with a power density of 100 mW cm^{-2} for 10 min at room temperature. Given its high sensitivity to singlet oxygen ($^1O_2$), 60 μL of disodium 9,10-anthracendipropionic acid (Na$_2$-ADPA, 1 mg mL^{-1}) was utilized to detect the $^1O_2$ generation by free acidic H$_2$O$_2$, free CDs/MnO$_2$-PEG, and CDs/MnO$_2$-PEG nanohybrids with or without the addition of H$_2$O$_2$ (100 μmol L^{-1}) at pH 6.5 under light irradiation. The produced $^1O_2$ was measured based on the amount of reduced Na$_2$-ADPA absorbance (excitation: 378 nm). In addition, electron spin-resonance spectroscopy (ESR) was performed to qualitatively detect the $^1O_2$ generation by CDs/MnO$_2$-PEG nanohybrids in the presence of acidic H$_2$O$_2$ under N$_2$ atmosphere. 2,2,6,6-Tetramethylpiperidine 1-oxyl was used as the $^1O_2$ capturing agent in the two groups.

Cellular experiments

CDs/MnO$_2$-PEG incubated *in vitro* with HeLa cells were subjected to imaging. All cells were cultured in normal DMEM medium containing 10% fetal bovine serum (FBS) and 1% penicillin/streptomycin at 37°C under 5% CO$_2$. The cells were seeded in 35 mm cell culture dishes and stimulated with a PBS solution of CDs/MnO$_2$-PEG (50 μg mL^{-1}). After being incubated for 4 h, the cells were washed with PBS twice to remove non-specifically bound CDs/MnO$_2$-PEG. Changes in fluorescence were then observed after acidic H$_2$O$_2$ (100 μmol L^{-1}) was added.

Images were captured using a Nikon C1silaser scanning confocal microscope, which can provide different atmospheres (air or N$_2$).

To detect $^1O_2$ generation *in vitro*, two groups of HeLa cells were incubated with CDs/MnO$_2$-PEG (200 μg mL^{-1}) at 37°C under 5% CO$_2$. After 4 h, one group was mixed with PBS containing acidic H$_2$O$_2$ (100 μmol L^{-1}), and the other group was added with a PBS solution with a normal physiological pH. The cells were then incubated with 2,7-dichlorodi-hydrofluoresce in diacetate (DCFH-DA, 1 mg mL^{-1}, 2 μL) for 10 min prior to observation. Cells incubated only with DCFH-DA served as the control group.

For the cell cytotoxicity assay, the cells were seeded into a 96-well plate with a density of 5×10^4 cells per well until the cells adhered and were then incubated with increasing concentrations (12.5, 25, 50, 100, 150, and 200 μg mL^{-1}) of CDs/MnO$_2$-PEG with or without acidic H$_2$O$_2$. After being incubated for 24 h in the dark, the standard thiazolyl tetrazolium (MTT) test was conducted to evaluate the cell viabilities relative to the untreated cells.

For PDT, HeLa cells seeded in 96-well plates were incubated with various concentrations of CDs/MnO$_2$-PEG for 4 h. The 96-well plates were placed in a glove box that had been ventilated under N$_2$ atmosphere in advance. This setup was maintained for 30 min before being exposed to 635 nm irradiation at a power density of 100 mW cm^{-2} for 30 min under circulating N$_2$. Then, the

cells were transferred into fresh media and further incubated for 24 h. Then the standard MTT test was conducted to evaluate the cell viability.

Calcein AM and propidium iodide (PI) assays were performed to verify the PDT effect of the CDs/MnO$_2$-PEG nanoparticles. Two groups of HeLa cells were mixed with CDs/MnO$_2$-PEG (200 µg mL^{-1}) at 37°C under 5% CO$_2$ for 4 h. Then, the cells were stored in a glove box and exposed to N$_2$ for 30 min. One group was supplemented with PBS containing H$_2$O$_2$ (100 µmol L^{-1}) at pH 6.5, and the other group was added with PBS with a normal physiological pH. Afterward, both groups were exposed to 635 nm irradiation at a power density of 100 mW cm^{-2} for 0, 3, 6 and 10 min under circulating N$_2$. The cells were co-stained with AM/PI for 10 min and washed with PBS twice prior to observation. Cells were only irradiated with 635 nm (100 mW cm^{-2}) laser served as the control group. Images were captured with a Nikon C1silaser scanning confocal microscope.

Animal modal
Female nude mice (15–20 g) were purchased from the Center for Experimental Animals, Institute of Process Engineering, CAS in Beijing, China. The procedures for the *in vivo* analyses were approved by the China Committee for Research and Animal Ethics in compliance with the law on animal experimentation. The tumor was induced through the subcutaneous injection of 2×10^6 murine breast cancer 4T1-luc cells in PBS (60 µL) into the right front paw of each mouse. The tumors were allowed to grow for 10 d to reach an approximate size of 100 mm^3.

For the *in vivo* MRI, CDs/MnO$_2$-PEG (1 mg mL^{-1}, 200 µL) were intravenously (i.v.) injected into the 4T1 tumor-bearing nude mice. After 24 h, MRI of the mice was performed with a 7T MRI scanner (Micro MRI, Varian 7T) at different time points (0, 4, 12 and 24 h).

Fluorescence scans were then performed at various time points (0, 4, 8, 12 and 24 h) post-injection (p.i.) with the use of a Maestro 2 Multispectral Small-animal Imaging System with a 635-nm laser as the excitation source.

To quantitatively evaluate the biodistribution of CDs/MnO$_2$-PEG, three tumor-bearing mice were sacrificed at different time intervals p.i. (4 h, 12 h, 24 h, 2 d, 7 d, 14 d and 28 d). The major organs and tissues (i.e., liver, spleen, kidney, heart, lung and the tumor) were weighed, digested, and solubilized in chloroazotic acid under heating for 2 h. After the organic compounds were completely oxidized, each sample was diluted to 10 mL with deionized water. The relative contents of Mn in the different samples were measured thrice by inductively coupled plasma mass spectrometry (ICP-MS).

In vivo O$_2$ generation was detected by using a photoacoustic (PA) tomography system with an excitation wavelength of 680 nm to measure the oxygenated hemoglobin (HBO$_2$) content at different time points (0, 4, 8, 12, and 24 h) after the i.v. administration of CDs/MnO$_2$-PEG (1 mg mL^{-1}, 200 µL). Oxygenation inside the tumor was reflected by the changes in HBO$_2$ content.

For *in vivo* PDT, the tumor-bearing nude mice were randomly divided into four groups (each group consisting of five mice): (1) without any treatment; (2) 635 nm laser irradiation (100 mW cm^{-2}) only; (3) intravenous injection of CDs/MnO$_2$-PEG (1 mg mL^{-1}, 200 µL) only; (4) i.v. injection of CDs/MnO$_2$-PEG (1 mg mL^{-1}, 200 µL) and 635 nm laser (100 mW cm^{-2}, 10 min). After being to the different treatments, the tumor volumes were measured by a caliper every 2 d. Tumor size and body weight were monitored every 2 d after treatment. The tumor volume was calculated by the equation: $V = ab^2/2$, where a and b denote the length and width of the tumor, respectively.

Histopathological examination
The tissues (i.e., heart, liver, spleen, kidney and lung) at 30 d p.i. of CDs/MnO$_2$-PEG and the tumors of the four groups at 1 d post-treatment were harvested and fixed in 4% formalin solution. Histopathological examinations were performed in accordance with standard laboratory procedures. The tissue or tumor samples were numbered and given blindly to a pathologist for conventional processing and analysis. All samples were embedded in paraffin blocks, sectioned into 4 µm slices, and mounted onto glass slides. The sections were stained with hematoxylin and eosin (H&E) prior to observation, and images were captured by an optical microscope.

RESULTS AND DISCUSSION

Characterization of CDs/MnO$_2$-PEG
After the CDs and KMnO$_4$ underwent a redox reaction, X-ray photoelectron spectroscopy (XPS) was performed to assess the compositions of the resulting samples. The survey spectrum in Fig. S1 indicated the presence of C, Mn and O. As shown in Fig. 1a, the deconvolution of the high-resolution XPS spectra of Mn 2p revealed two peaks at 642.2 and 653.9 eV, which corresponded to the Mn (IV) 2p$_{2/3}$ and Mn(IV) 2p$_{1/2}$ spin-orbit peaks, respectively, of Mn^{4+} with a spin-energy separation of 11.7 eV [53]. This phenomenon confirmed that the positively charged CDs reduced KMnO$_4$ into MnO$_2$. To improve their stability, the obtained CDs/MnO$_2$ composites were modified
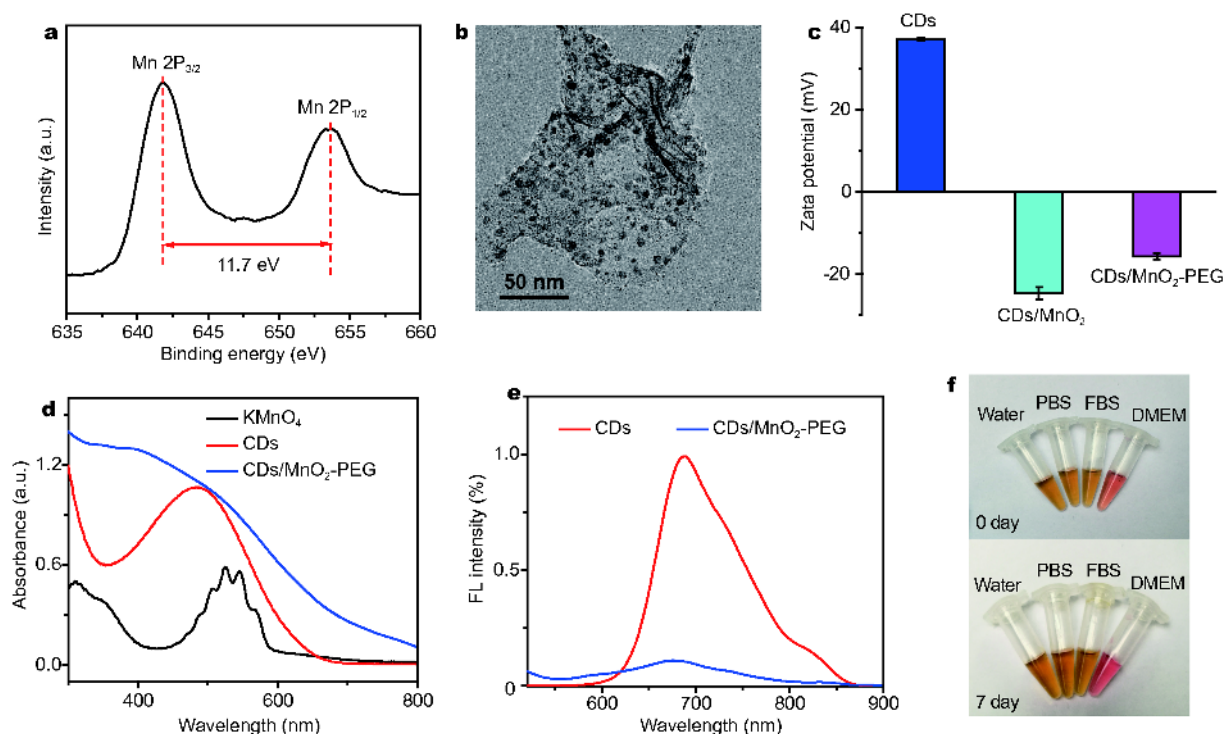
Figure 1 Characterizations of CDs/MnO$_2$-PEG nanohybrids. (a) XPS spectrum of CDs/MnO$_2$ nanohybrids. (b) A TEM image of CDs/MnO$_2$-PEG nanohybrids (scale bar: 200 nm). (c) Zeta potentials of CDs, CDs/MnO$_2$, and CDs/MnO$_2$-PEG. (d) UV-vis spectra of KMnO$_4$, CDs, and CDs/MnO$_2$-PEG. (e) FL spectra of CDs/MnO$_2$-PEG and CDs. (f) Optical photographs of CDs/MnO$_2$-PEG in water, PBS, FBS, and DMEM at 0 d (top) and 7 d (bottom).

with aminoterminated PEG ($M_w \approx 2,000$) through Mn–N coordinate bonding (Fig. S2) [54]. As revealed by transmission electron microscopy (TEM) in Fig. 1b, the CDs/MnO$_2$-PEG nanohybrids displayed an approximate average size of 180 nm. The high-resolution TEM image of the CDs loaded onto MnO$_2$ (Fig. S3a) revealed that the inter planar distance was approximately 0.31 nm, indicating that the reacted CDs retained their original crystallinity. Energy-dispersive X-ray spectroscopy spectrum also proved that the elements (i.e., Mn, C, O, etc.) were present in the CDs/MnO$_2$-PEG nanohybrids (Fig. S3b). As shown in Fig. 1c, the zeta potential changed from +37.1 mV for CDs to −21.7 mV for CDs/MnO$_2$ because of the formation of hydrogen bonds in the aqueous solution and the transformation of the surface charge by the MnO$_2$ nanoparticles. After being stirred with aminoterminated PEG, the zeta potential of the CDs/MnO$_2$-PEG nanohybrids increased to −17.9 mV, indicating the successful formation of CDs/MnO$_2$-PEG nanohybrids, which were favorable for long blood circulation.

UV-vis spectra (Fig. 1d) revealed that the four characteristic peaks of KMnO$_4$ (between 500 and 550 nm) disappeared after the reaction in the presence of the po-

sitively charged CD PDT agent. However, a new broad absorbance band appeared in the range of 300–800 nm, implying the surface plasmon band of generated MnO$_2$. As shown in Fig. 1e, the fluorescence of the CDs at the maximum emissive peak of 690 nm was significantly absorbed by the MnO$_2$ because of the significant overlap between the emission spectrum of CDs and the absorption spectrum of MnO$_2$. This phenomenon suggested the CDs/MnO$_2$-PEG nanohybrids displayed faint fluorescence signal under normal physiological conditions. The loading efficiency of CDs onto CDs/MnO$_2$-PEG was evaluated by obtaining the UV-vis spectra of the CDs at 492 nm. The maximum loading efficiency reached up to approximately 65% (Fig. S4). In addition, the obtained CDs/MnO$_2$-PEG was highly dispersible and stable in water, PBS, FBS, and DMEM. No obvious aggregation was observed even after a prolonged time of 7d (Fig. 1f).

pH/H$_2$O$_2$-responsive CDs/MnO$_2$-PEG nanohybrids
In neutral solutions (pH 7.4), MnO$_2$ catalyzed the disproportionation reaction of H$_2$O$_2$ into H$_2$O and O$_2$ [27]. By contrast, in acid solutions of H$_2$O$_2$ (pH 6.5), H$_2$O$_2$ was oxidized to oxygen while MnO$_2$ nanoparticles were bro-
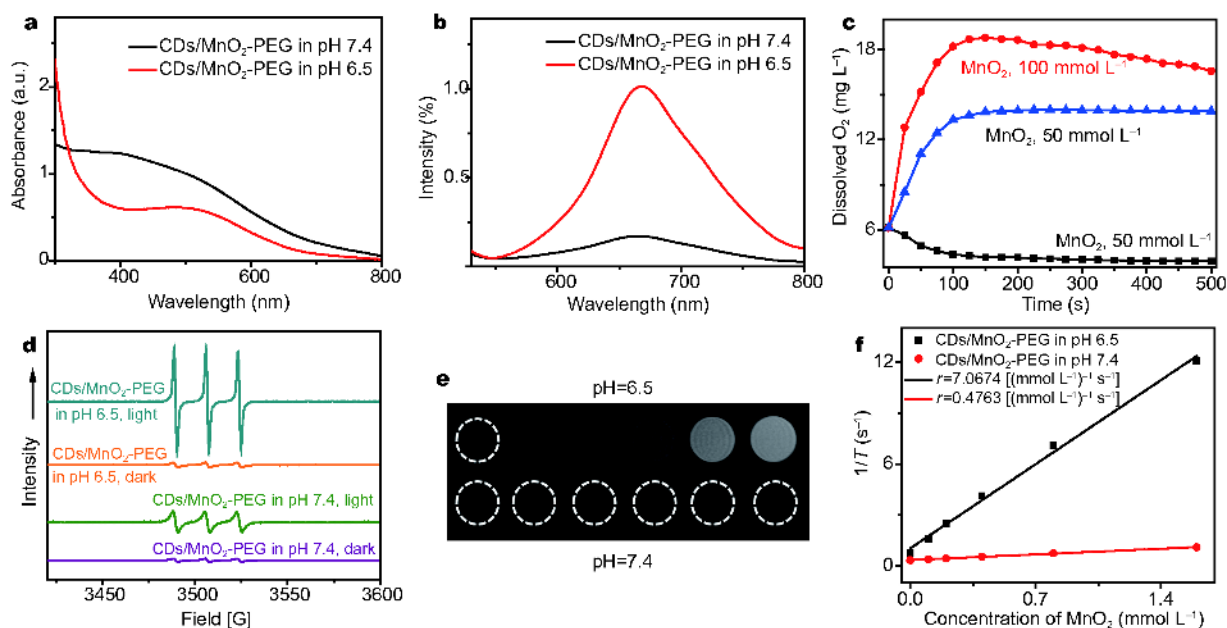
Figure 2 pH/HO$_2$-response of CDs/MnO$_2$-PEG nanohybrids. (a) UV-vis-NIR spectra and (b) FL spectra of CDs/MnO$_2$-PEG nanohybrids at pH 6.5 and 7.4, respectively. (c) Simultaneous O$_2$ generation in acidic H$_2$O$_2$ solutions (10 mmol L^{-1}) after adding different concentrations of (MnO$_2$: 0, 50, and 100 mmol L^{-1}) of CDs/MnO$_2$-PEG. (d) Characteristic ^{1}O$_2$-induced signal in the ESR spectra after 635 nm laser irradiation (100 mW cm^{-2}) under N$_2$ atmosphere, in the absence of presence of H$_2$O$_2$ (100 µmol L^{-1}). (e) T1-weighted MR images of various concentrations of CDs/MnO$_2$-PEG solutions incubated at different pH values (7.4 and 6.5) for 6 h prior to MRI. (f) Concentration-dependent T1 relaxation rates. The longitudinal relaxivities (r1) were determined to be 0.4763 and 7.0674 (mmol L^{-1})$^{-1}$ s^{-1} for CDs/MnO$_2$-PEG nanohybrids at pH 7.4 and 6.5, respectively.

ken down and Mn^{4+} was rapidly reduced into colorless Mn^{2+} [55–58], leading to the release of CDs, as the following reaction (1)

$$MnO_2 + H_2O_2 + 2H^+ \rightarrow Mn^{2+} + 2H_2O + O_2 \uparrow. \qquad (1)$$

As shown by the comparison of the absorption and fluorescence spectra of CDs/MnO$_2$-PEG at pH 7.4 and 6.5 in Fig. 2a and b, the initial absorption spectrum of the CDs appeared, and the markedly enhanced FL intensity of the CDs was also observed. Then, dissolved O$_2$ in the reacted solution was quantitatively tested by an oxygen probe (ST300D, portable Dissolved Oxygen Meters, Chang zhou OHAUS Instrument Factory) with increasing concentrations of CDs/MnO$_2$-PEG nanohybrids (MnO$_2$: 0, 50, 100 mmol L^{-1}) which resulted in the rapid generation of oxygen in acidic H$_2$O$_2$ (10 mmol L^{-1}) as shown in Fig. 2c, and gas bubbles were clearly observed at 100 mmol L^{-1} of H$_2$O$_2$ (Fig. S5). These findings indicated that the CDs/MnO$_2$-PEG can be used for the quantitative detection of acidic H$_2$O$_2$ by examining the FL intensity of CDs and the production of oxygen. As shown in Fig. S6, the size of CDs/MnO$_2$-PEG nanohybrids also changed from ~180 nm (at pH 7.4) to 5–20 nm (at pH 6.5), indicating the decomposition of MnO$_2$ nanoparticles in the

acidic condition.

The capability of the CDs/MnO$_2$-PEG nanohybrids to produce ^{1}O$_2$ in response to acidic H$_2$O$_2$ was investigated. Specifically, the ^{1}O$_2$ generation of the CDs/MnO$_2$-PEG nanohybrids upon 635 nm irradiation with or without 100 µmol L^{-1} acidic H$_2$O$_2$ (pH 6.5) was tested by using Na$_2$-ADPA as an indicator. As shown in Fig. S7, without the addition of H$_2$O$_2$, slight ^{1}O$_2$ generation was observed because of the CDs quenching by MnO$_2$. However, the markedly decreased ADPA absorption at 378 nm implied that more ^{1}O$_2$ were generated after acidic H$_2$O$_2$ was added. In the acidic H$_2$O$_2$ solution (pH 6.5), the recovered emission of the CDs resulted in the further enhancement of ^{1}O$_2$ generation because of the dissociation and reduction of MnO$_2$ by the acidic H$_2$O$_2$. Then, ESR was used to measure the light-responsive ^{1}O$_2$ generation of the CDs/MnO$_2$-PEG nanohybrids under N$_2$ atmosphere. As shown in Fig. 2d, the CDs/MnO$_2$-PEG nanohybrids exhibited a strong ESR signal only upon 635 nm laser irradiation (100 mW cm^{-2}) with the addition of acidic H$_2$O$_2$, indicating the efficient ^{1}O$_2$ production under such conditions. By contrast, no obvious ^{1}O$_2$ generation was observed under neutral conditions (pH 7.4), suggesting that the significantly improved PDT efficiency of the
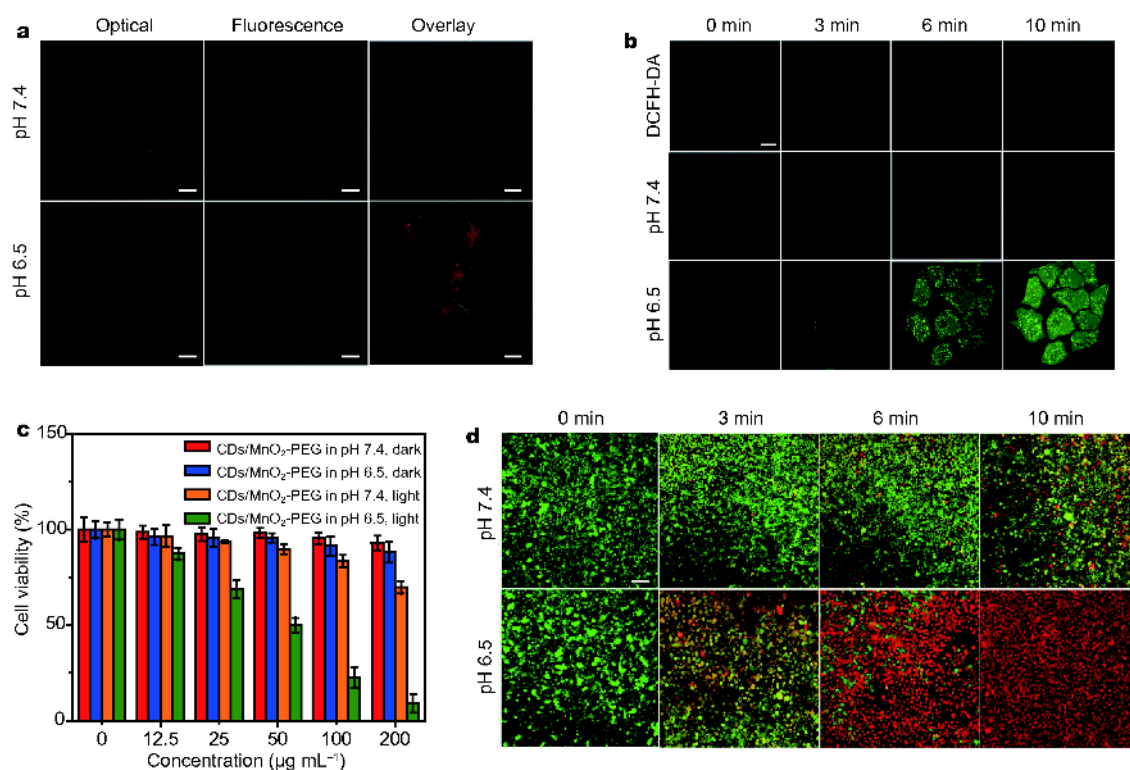
Figure 3 *In vitro* imaging and PDT. (a) Confocal microscopy images of HeLa cells incubated with CDs/MnO$_2$-PEG nanohybrids (200 µg mL^{-1}) for 4 h and added with acidic H$_2$O$_2$ at a bright field and excitation at 635 nm (scale bar: 10 µm). (b) Confocal images of HeLa cells incubated with DCFH-DA, CDs/MnO$_2$-PEG nanohybrids at pH 7.4 and 6.5 at different irradiation times (0, 3, 6, 10 min). (c) Relative viabilities of HeLa cells after incubation with CDs/MnO$_2$-PEG nanohybrids for 24 h in the dark, at pH 7.4 and 6.5 upon light irradiation (635 nm,100 mW cm^{-2}, 10 min) under N$_2$ atmosphere, respectively. (d) Fluorescence images of calcein AM and PI co-stained HeLa cells incubated with CDs/MnO$_2$-PEG nanohybrids (200 µg mL^{-1}) at pH 7.4 and 6.5 with 635 nm irradiation (100 mW cm^{-2}) for 0, 3, 6 and 10 min (scale bar: 150 µm).

CDs/MnO$_2$-PEG nanohybrids was due to the enhanced O$_2$ generation resulting from the MnO$_2$-catalyzed decomposition of H$_2$O$_2$ under hypoxia.

The T1-weighted MRI of the CDs/MnO$_2$-PEG nanohybrids were further examined under neutral (pH 7.4) and acidic conditions (pH 6.5). As shown in Fig. 2e and f, the as-prepared CDs/MnO$_2$-PEG nanohybrids displayed concentration-dependent T1-weighted MRI signals under both neutral and acidic conditions. However, the CDs/MnO$_2$-PEG nanohybrids under acidic conditions (pH 6.5) exhibited a more strongly enhanced T1-weighted MRI than those under neutral conditions (pH 7.4) because of the reduction of MnO$_2$ into Mn^{2+} by the acidic H$_2$O$_2$ [59]. The r1 value of the CDs/MnO$_2$-PEG nanohybrids drastically increased from 0.4763 (mmol L^{-1})$^{-1}$ s^{-1} under neutral conditions (pH 7.4) to 7.0674 (mmol L^{-1})$^{-1}$ s^{-1} under acidic conditions (pH 6.5), thereby enhancing the r1 value by 15-fold in the presence of H$_2$O$_2$/H$^+$. This finding indicated the potential of a MRI-guided PDT of solid tumors. Thus, CDs/MnO$_2$-PEG can act as a pH/H$_2$O$_2$-

driven, turn-on nanotheranostics for the multimodal imaging-guided PDT of cancer.

In vitro imaging and PDT

In vitro experiments were conducted to determine whether the as-prepared CDs/MnO$_2$-PEG nanohybrids can serve as an effective, pH/H$_2$O$_2$-driven, turn-on nanotheranostics for the multimodal imaging-guided PDT of cancer. Confocal images (Fig. 3a) showed that HeLa cells treated with CDs/MnO$_2$-PEG nanohybrids under neutral conditions (pH 7.4) exhibited weak fluorescence because of the quenching effect of MnO$_2$ nanoparticles on CDs. However, the fluorescent signals of CDs were significantly increased after acidic H$_2$O$_2$ was added because of the MnO$_2$ nanoparticles were disintegrated [60], thereby releasing of the red emissive CDs. Z-Stack imaging further demonstrated that the CDs/MnO$_2$-PEG nanohybrids were localized in the cytoplasm rather than the cell membrane (Fig. S8). These results proved that the as-prepared CDs/MnO$_2$-PEG nanohybrids can be applied as

a pH/H_2O_2-responsive, turn-on fluorescence imaging agent *in vitro*.

To further investigate the *in vitro* PDT effect of the CDs/MnO_2-PEG nanohybrids under a TEM with acidic H_2O_2 conditions (pH 6.5), the capability of CDs/MnO_2-PEG nanohybrids for $^1O_2$ generation was examined *in vitro*. 2,7-Dichlorodi-hydrofluorescein diacetate (DCHF-DA), which is a standard FL indicator for ROS, was used to track $^1O_2$ generation under N_2 atmosphere. As shown in Fig. 3b, the cells incubated with CDs/MnO_2-PEG nanohybrids under neutral condition (pH 7.4) displayed week fluorescence under N_2, implying that scarce $^1O_2$ production occurred. However, under acidic conditions, the green fluorescence was further enhanced by continuous incubation for 10 min, indicating that was effectively generated.

An *in vitro* viability assay was performed on HeLa cells under N_2 atmosphere to investigate the PDT effect of CDs/MnO_2-PEG nanohybrids. As shown in Fig. 3c, the CDs/MnO_2-PEG nanohybrids exhibited negligible adverse effects on the viabilities of the HeLa cells at the tested concentrations ranging from 6.25 to 200 μg mL^{-1} with or without acidic H_2O_2, thus indicating the favorable biocompatibility of the CDs/MnO_2-PEG nanohybrids. However, in the presence of acidic H_2O_2 (pH 6.5), a significant concentration-dependent cytotoxicity of the CDs/MnO_2-PEG nanohybrids was observed, and a 95% inhibitory effect was achieved at 200 μg mL^{-1} of CDs/MnO_2-PEG nanohybrids upon 635 nm laser irradiation. By contrast, the cell viability slightly decreased at pH 7.4. The *in vitro* PDT effect of the CDs/MnO_2-PEG nanohybrids under a TME with acidic H_2O_2 conditions (pH 6.5) under N_2 atmosphere was verified by conducting a calcein AM and PI co-staining assay. The observed green fluorescence indicated that few cell deaths occurred at pH 7.4 even after the irradiation time was prolonged to 10 min (Fig. 3d). However, at pH 6.5, a homogeneous red fluorescence was observed at 200 μg mL^{-1} of the CDs/MnO_2-PEG nanohybrids upon 635 nm laser irradiation, indicating complete cell death. These *in vitro* results suggested that CDs/MnO_2-PEG can act as an effective pH/H_2O_2-driven, turn-on nanotheranostics for the imaging-guided PDT of cancer under an acidic and hypoxia TME.
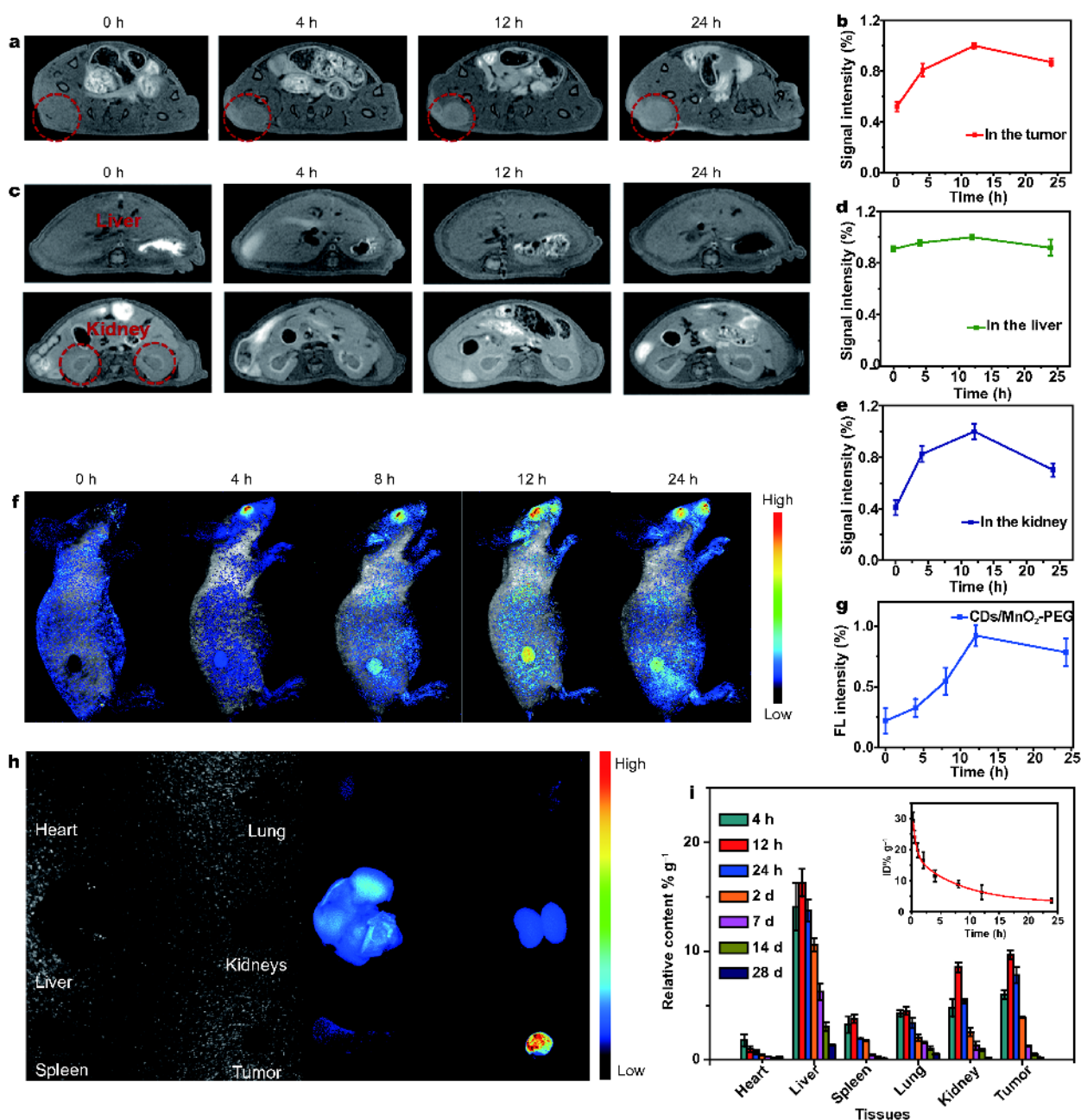
In vivo MR/FL imaging and real-time biodistribution

To investigate the feasibility of CDs/MnO_2-PEG nanohybrids for *in vivo* MRI, mice bearing subcutaneous 4T1 tumors of approximately 100 mm^3 were selected as models. *In vivo* MRI was performed at different times (0, 4, 12, and 24 h) with the use of a 7T MR scanner. As shown in Fig. 4a and b, a weak MR signal was observed in the tumor site at 4 h p.i. of CDs/MnO_2-PEG nanohybrids. This finding indicated that the CDs/MnO_2-PEG nanohybrids accumulated in the tumor area because of the enhanced permeability and retention (EPR) effect and the gradual reduction of MnO_2 into Mn^{2+} in the mildly acidic TME [61,62]. The MR signal intensity at the tumor site reached a fastigium at 12 h p.i. and decreased at 24 h p.i. The T1 signals observed in the kidneys reached their maximum at 12 h p.i. (Fig. 4c–e), suggesting the renal clearance of the Mn^{2+} decomposed from MnO_2. By contrast, no obvious T1 signal changes were observed in the liver because of its neutral environment.

Subsequently, the FL imaging of a tumor-bearing mouse was conducted *in vivo* at different time intervals after the i.v. injection of CDs/MnO_2-PEG nanohybrids (1 mg mL^{-1}, 200 μL). Fig. 4f and g show that the FL intensity at the tumor site rapidly increased within 12 h p.i., and then plateaued. *Ex vivo* imaging of major organs and tumors collected from mice at 12 h p.i. was further examined. As shown in Fig. 4h, the excised tumor tissue displayed strong FL intensity, whereas the liver and the kidney presented very low signals. These findings agreed well with the *in vivo* MRI behavior. Therefore, both MR and FL imaging indicated that 12 h p.i. was the optimal time for the subsequent PDT. And the CDs/MnO_2-PEG nanohybrids were responsive only in the TME but maintained an "off" state in normal physiological environments, suggesting that CDs/MnO_2-PEG nanohybrids can be used as a tumor-targeted, multifunctional theranostic for eliminating the damage toward normal tissues during PDT.

The real-time biodistribution of CDs/MnO_2-PEG nanohybrids at different times was examined by ICP-MS, which is a sensitive method that can accurately detect the content of Mn in different organs. For *ex vivo* analyses, tumor-bearing mice were i.v. injected with CDs/MnO_2-PEG nanohybrids (1 mg mL^{-1}, 200 μL) and then sacrificed at different time intervals (1 h, 12 h, 24 h, 2 d, 7 d, 14 d, and 28 d) to harvest the tumors. Fig. 4i illustrates the trends of biodistribution and metabolic clearance of the Mn ions in the tumors. Analysis of the statistical results revealed that CDs/MnO_2-PEG nanohybrids accumulated in the tumor through the EPR effect. This accumulation increased within 1–12 h p.i., plateaued at 12 h p.i., and then steadily decreased over time. In addition, CDs/MnO_2-PEG nanohybrids also accumulated in the liver, the lungs, the kidneys, the spleen, and the heart; the accumulation likewise steadily decreased over time,

Figure 4 *In vivo* MR/FL imaging and biodistribution. (a) Time-dependent T1-weighted MR images (transverse section) and (b) T1-weighted MR signals of the tumor. (c) *In vivo* T1-weighted MR images (transverse section) of the kidney and liver in the same mouse. (d) T1-weighted MR signals of the liver in the same mouse. (e) T1-weighted MR signals of the kidney in the same mouse. (f) Time-dependent FL images of tumor-bearing nude mouse after an i.v. injection of CDs/MnO$_2$-PEG nanohybrids (1 mg mL^{-1}, 200 μL). (g) FL signals in the tumor before, 4, 8, 12, and 24 h p.i. of CDs/MnO$_2$-PEG nanohybrids. (h) *Ex vivo* FL images of major organs and tumor dissected from the same mice at 12 h p.i. tumor, liver, spleen, kidney, heart and lung. (i) Time-dependent content of Mn in the *ex vivo* tumor and other organs after an i.v. injection of CDs/MnO$_2$-PEG nanohybrids. Inset is the blood circulation curve of the CDs/MnO$_2$-PEG nanohybrids in mice that was measured based on the content of Mn in blood at different time points p.i. Error bars are based on the standard deviation of three mice.

resulting in the complete removal of the CDs/MnO$_2$-PEG nanohybrids from the main organs and tumors after 4 weeks.

To evaluate the blood circulation of the CDs/MnO$_2$-PEG nanohybrids, blood samples of tumor-bearing mice were extracted at various time points (15 min, 30 min,
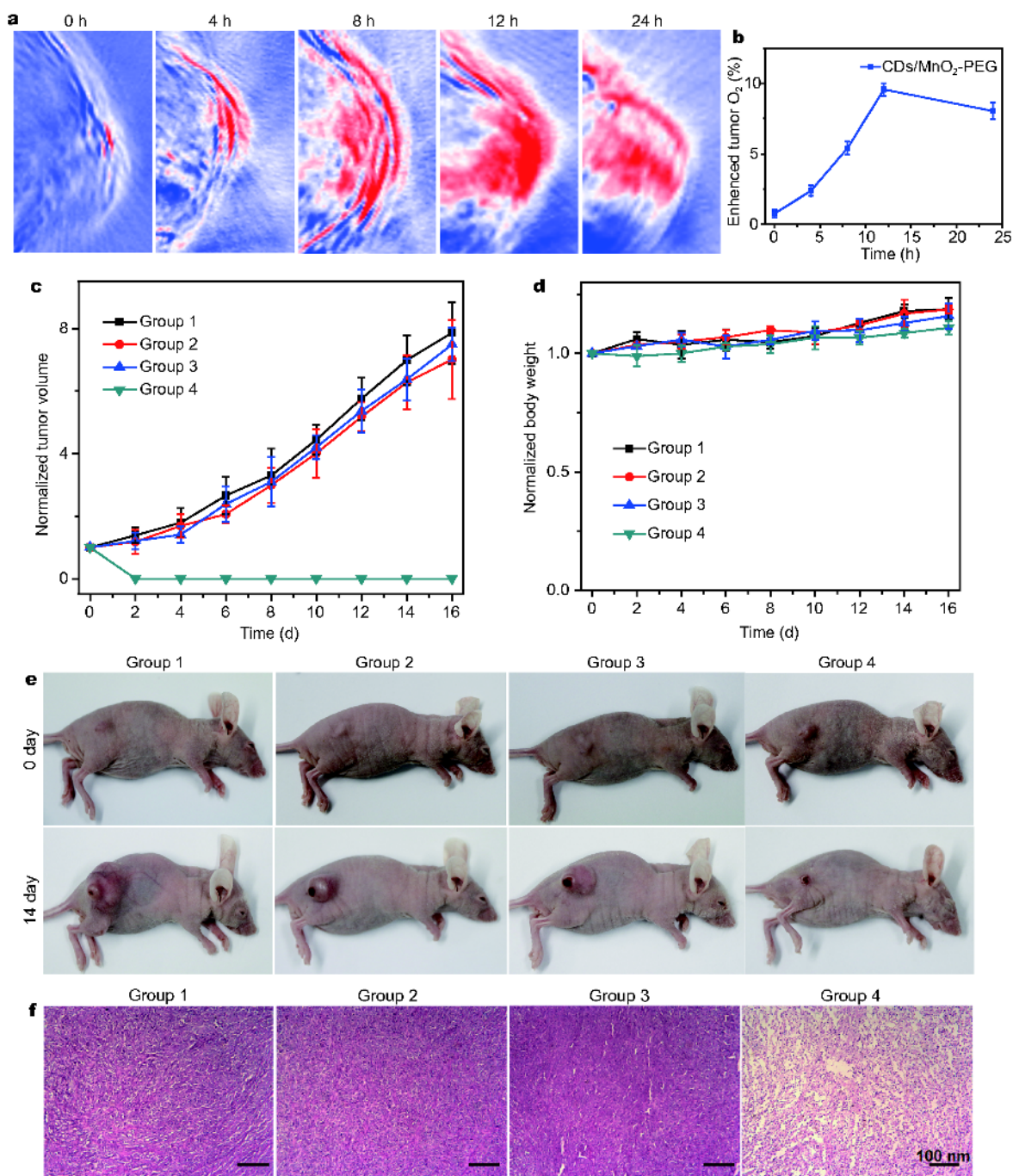
Figure 5 *In vivo* PDT. (a) PA images of 4T1 solid tumors measured based on HBO$_2$ at different time points p.i. of CDs/MnO$_2$-PEG nanohybrids. (b) Average enhanced tumor vascular saturated O$_2$ p.i. of CDs/MnO$_2$-PEG nanohybrids. (c) Time-dependent tumor growth curves of mice ($n = 5$) observed after various treatments. (d) Relative body weights of the nude mice after different treatments. (e) Representative photographs of the four groups after different treatments. (f) H&E-stained tumor slices from different groups collected 24 h after light irradiation. (scale bar: 100 μm).

1 h, 2 h, 4 h, 8 h, 12 h, 24 h) p.i. and then quantitatively measured by ICP-MS to precisely determine the Mn content in the blood. As shown by the inset in Fig. 4i, the blood level of CDs/MnO$_2$-PEG decreased gradually over time, as in a two-compartment model. Then, secondary exponential fitting was utilized to calculate the first ($t_{1/2}$

(a)) and second ($t_{1/2}$ (b)) phases of the circulation half-lives, which were approximately 0.57 and 8.15 h, respectively. Such long blood circulation of CDs/MnO$_2$-PEG nanohybrids should be favorable for effective tumor accumulation.

In vivo O$_2$-enhanced PDT

To further demonstrate the ability of CDs/MnO$_2$-PEG nanohybrids to ameliorate tumor hypoxia, PA imaging was performed to detect HBO$_2$ content in the tumors at different time points after the i.v. injection of the CDs/MnO$_2$-PEG nanohybrids. As shown in Fig. 5a and b, the mean intensities of the HBO$_2$ signs increased with time and reached a maximum value at approximately 12 h p.i., indicating the successful alleviation of tumor hypoxia due to the MnO$_2$-triggered decomposition of H$_2$O$_2$ into O$_2$. Such enhanced oxygenation in the TME was favorable for increasing the efficiency of *in vivo* PDT. Then, the *in vivo* PDT efficacy of the CDs/MnO$_2$-PEG nanohybrids was evaluated. Balb/c mice bearing subcutaneous 4T1 tumors were divided into four groups: Group 1: without any treatment; Group 2: laser irradiation only; Group 3: CDs/MnO$_2$-PEG nanohybrids (1 mg mL^{-1}, 200 μL) without laser irradiation; Group 4: CDs/MnO$_2$-PEG nanohybrids (1 mg mL^{-1}, 200 μL) with laser irradiation. At 12 h p.i., the mice in Groups 2 and 4 were irradiated by 635 nm laser (100 mW cm^{-2}, 10 min). The tumor volumes of all the mice were measured by a caliper every 2 d. As shown in Fig. 5c, the mice in Group 4 exhibited a significant suppression of tumor growth, demonstrating a remarkably improved therapeutic efficacy. By contrast, all tumor tissues of the mice in Groups 1, 2, and 3 continued to grow (Fig. 5e). The *in vivo* toxicity of the CDs/MnO$_2$-PEG nanohybrids was also investigated by monitoring the weight change of the mice during the study period. As shown in Fig. 5d, no abnormal changes were observed in any of the groups, indicating the absence of acute toxicity of the CDs/MnO$_2$-PEG nanohybrids *in vivo*.

The microscopy images of the H&E-stained tumor slices further revealed that the PDT triggered by CDs/MnO$_2$-PEG nanohybrids severely damaged the tumor cells, whereas the tumor cells in the control groups mostly retained their regular morphology (Fig. 5f). The H&E-stained slices of the main organs (heart, liver, spleen, lung and kidney) were also evaluated for histology analysis at 30 d post i.v. injection of CDs/MnO$_2$-PEG nanohybrids. Compared with the cells of a healthy mouse, those in the examined tissues retained their normal morphology (Fig. S9), showing neither significant inflammation nor damage. Overall, these results illustrate that CDs/MnO$_2$-

PEG nanohybrids are a highly effective, scarcely biotoxic PDT agent *in vivo*.

CONCLUSIONS

In summary, pH/H$_2$O$_2$-responsive CDs/MnO$_2$-PEG nanohybrids were successfully synthesized *via* the redox reaction between the CD PDT agent and KMnO$_4$ followed by PEGylation. The as-prepared CDs/MnO$_2$-PEG nanohybrids possessed the following characteristics: (1) quenched fluorescence, weak singlet oxygen generation, and low MRI signal in the normal physiological environment; (2) synchronously enhanced fluorescence, singlet oxygen generation, and MRI signal in the tumor microenvironment; and (3) low toxicity and complete clearance from the body. *In vitro* and *in vivo* analyses reveal that the low-toxic CDs/MnO$_2$-PEG nanohybrids can be applied as pH/H$_2$O$_2$-driven, turn-on nanotheranostics for the concurrent bimodal MR/FL imaging and oxygen-elevated PDT of solid tumors if the TME is regulated. This work offers a new nanotheranostic candidate for modulating the unfavorable TME, particularly for the targeted PDT of cancer through precise positioning and oxygen generation.

1   Kunjachan S, Ehling J, Storm G, *et al.* Noninvasive imaging of nanomedicines and nanotheranostics: principles, progress, and prospects. Chem Rev, 2015, 115: 10907–10937

2   Sun Q, Sun X, Ma X, *et al.* Integration of nanoassembly functions for an effective delivery cascade for cancer drugs. Adv Mater, 2014, 26: 7615–7621

3   Singh RK, Patel KD, Leong KW, *et al.* Progress in nanotheranostics based on mesoporous silica nanomaterial platforms. ACS Appl Mater Interfaces, 2017, 9: 10309–10337

4   Huang H, Lovell JF. Advanced functional nanomaterials for theranostics. Adv Funct Mater, 2017, 27: 1603524

5   Huo M, Wang L, Chen Y, *et al.* Tumor-selective catalytic nanomedicine by nanocatalyst delivery. Nat Commun, 2017, 8: 357

6   Shi J, Kantoff PW, Wooster R, *et al.* Cancer nanomedicine: progress, challenges and opportunities. Nat Rev Cancer, 2017, 17: 20–37

7   Anchordoquy TJ, Barenholz Y, Boraschi D, *et al.* Mechanisms and barriers in cancer nanomedicine: addressing challenges, looking for solutions. ACS Nano, 2017, 11: 12–18

8   Ma Y, Li X, Li A, *et al.* H$_2$S-activable MOF nanoparticle photosensitizer for effective photodynamic therapy against cancer with controllable singlet-oxygen release. Angew Chem Int Ed, 2017, 56: 13752–13756

9   Hu D, Sheng Z, Gao G, *et al.* Activatable albumin-photosensitizer nanoassemblies for triple-modal imaging and thermal-modulated photodynamic therapy of cancer. Biomaterials, 2016, 93: 10–19

10 Luo D, Carter KA, Razi A, *et al.* Doxorubicin encapsulated in stealth liposomes conferred with light-triggered drug release. Biomaterials, 2016, 75: 193–202

11 Lucky SS, Soo KC, Zhang Y. Nanoparticles in photodynamic therapy. Chem Rev, 2015, 115: 1990–2042

12 Yuan Y, Zhang CJ, Gao M, et al. Specific light-up bioprobe with aggregation-induced emission and activatable photoactivity for the targeted and image-guided photodynamic ablation of cancer cells. Angew Chem Int Ed, 2015, 54: 1780–1786

13 Guo L, Liu W, Niu G, et al. Polymer nanoparticles with high photothermal conversion efficiency as robust photoacoustic and thermal theranostics. J Mater Chem B, 2017, 5: 2832–2839

14 Xing R, Liu K, Jiao T, et al. An injectable self-assembling collagen-gold hybrid hydrogel for combinatorial antitumor photothermal/photodynamic therapy. Adv Mater, 2016, 28: 3669–3676

15 Jia Q, Chen M, Liu Q, et al. Ethylene glycol-mediated synthetic route for production of luminescent silicon nanorod as photodynamic therapy agent. Sci China Mater, 2017, 60: 881–891

16 Wen R, Lv X, Yang T, et al. Albumin nanoreactor-templated synthesis of Gd_2O_3/CuS hybrid nanodots for cancer theranostics. Sci China Mater, 2017, 60: 554–562

17 Yu Z, Wang M, Pan W, et al. Tumor microenvironment-triggered fabrication of gold nanomachines for tumor-specific photoacoustic imaging and photothermal therapy. Chem Sci, 2017, 8: 4896–4903

18 Kanamala M, Wilson WR, Yang M, et al. Mechanisms and biomaterials in pH-responsive tumour targeted drug delivery: a review. Biomaterials, 2016, 85: 152–167

19 Mura S, Nicolas J, Couvreur P. Stimuli-responsive nanocarriers for drug delivery. Nat Mater, 2013, 12: 991–1003

20 Mou J, Chen Y, Ma M, et al. Facile synthesis of liposome/Cu_{2-x}S-based nanocomposite for multimodal imaging and photothermal therapy. Sci China Mater, 2015, 58: 294–301

21 Mathiyazhakan M, Upputuri PK, Sivasubramanian K, et al. In situ synthesis of gold nanostars within liposomes for controlled drug release and photoacoustic imaging. Sci China Mater, 2016, 59: 892–900

22 Dai Y, Xu C, Sun X, et al. Nanoparticle design strategies for enhanced anticancer therapy by exploiting the tumour microenvironment. Chem Soc Rev, 2017, 46: 3830–3852

23 Khawar IA, Kim JH, Kuh HJ. Improving drug delivery to solid tumors: Priming the tumor microenvironment. J Control Release, 2015, 201: 78–89

24 Wu T, Dai Y. Tumor microenvironment and therapeutic response. Cancer Lett, 2016, 387: 61–68

25 Cheng H, Zhu JY, Li SY, et al. An O_2 self-sufficient biomimetic nanoplatform for highly specific and efficient photodynamic therapy. Adv Funct Mater, 2016, 26: 7847–7860

26 Chen H, Tian J, He W, et al. H_2O_2-activatable and O_2-evolving nanoparticles for highly efficient and selective photodynamic therapy against hypoxic tumor cells. J Am Chem Soc, 2015, 137: 1539–1547

27 Chen Q, Feng L, Liu J, et al. Intelligent albumin-MnO_2 nanoparticles as pH-/H_2O_2-responsive dissociable nanocarriers to modulate tumor hypoxia for effective combination therapy. Adv Mater, 2016, 28: 7129–7136

28 Yang G, Zhang R, Liang C, et al. Manganese dioxide coated WS_2@Fe_3O_4/sSiO$_2$ nanocomposites for pH-responsive MR imaging and oxygen-elevated synergetic therapy. Small, 2018, 14: 1702664

29 Liu J, Chen Q, Zhu W, et al. Nanoscale-coordination-polymer-shelled manganese dioxide composite nanoparticles: a multistage redox/pH/H_2O_2-responsive cancer theranostic nanoplatform. Adv Funct Mater, 2017, 27: 1605926

30 Yuan F, Li S, Fan Z, et al. Shining carbon dots: Synthesis and

biomedical and optoelectronic applications. Nano Today, 2016, 11: 565–586

31 Lim SY, Shen W, Gao Z. Carbon quantum dots and their applications. Chem Soc Rev, 2015, 44: 362–381

32 Zhu S, Meng Q, Wang L, et al. Highly photoluminescent carbon dots for multicolor patterning, sensors, and bioimaging. Angew Chem Int Ed, 2013, 52: 3953–3957

33 Chen Y, Shi J. Mesoporous carbon biomaterials. Sci China Mater, 2015, 58: 241–257

34 Roy E, Patra S, Madhuri R, et al. Carbon dot/TAT peptide co-conjugated bubble nanoliposome for multicolor cell imaging, nuclear-targeted delivery, and chemo/photothermal synergistic therapy. Chem Eng J, 2017, 312: 144–157

35 Huang Q, Lin X, Zhu JJ, et al. Pd-Au@carbon dots nanocomposite: Facile synthesis and application as an ultrasensitive electrochemical biosensor for determination of colitoxin DNA in human serum. Biosens Bioelectron, 2017, 94: 507–512

36 Gao N, Yang W, Nie H, et al. Turn-on theranostic fluorescent nanoprobe by electrostatic self-assembly of carbon dots with doxorubicin for targeted cancer cell imaging, in vivo hyaluronidase analysis, and targeted drug delivery. Biosens Bioelectron, 2017, 96: 300–307

37 Ge J, Lan M, Liu W, et al. Graphene quantum dots as efficient, metal-free, visible-light-active photocatalysts. Sci China Mater, 2016, 59: 12–19

38 Wang Z, Yuan F, Li X, et al. 53% Efficient red emissive carbon quantum dots for high color rendering and stable warm white-light-emitting diodes. Adv Mater, 2017, 29: 1702910

39 Ong WJ, Putri LK, Tan YC, et al. Unravelling charge carrier dynamics in protonated g-C_3N_4 interfaced with carbon nanodots as co-catalysts toward enhanced photocatalytic CO_2 reduction: A combined experimental and first-principles DFT study. Nano Res, 2017, 10: 1673–1696

40 Huang P, Lin J, Wang X, et al. Light-triggered theranostics based on photosensitizer-conjugated carbon dots for simultaneous enhanced-fluorescence imaging and photodynamic therapy. Adv Mater, 2012, 24: 5104–5110

41 Choi Y, Kim S, Choi MH, et al. Highly biocompatible carbon nanodots for simultaneous bioimaging and targeted photodynamic therapy in vitro and in vivo. Adv Funct Mater, 2014, 24: 5781–5789

42 Zheng M, Liu S, Li J, et al. Integrating oxaliplatin with highly luminescent carbon dots: an unprecedented theranostic agent for personalized medicine. Adv Mater, 2014, 26: 3554–3560

43 Karthik S, Saha B, Ghosh SK, et al. Photoresponsive quinoline tethered fluorescent carbon dots for regulated anticancer drug delivery. Chem Commun, 2013, 49: 10471–10473

44 Zhang M, Wang W, Zhou N, et al. Near-infrared light triggered photo-therapy, in combination with chemotherapy using magnetofluorescent carbon quantum dots for effective cancer treating. Carbon, 2017, 118: 752–764

45 Fan Z, Zhou S, Garcia C, et al. pH-responsive fluorescent graphene quantum dots for fluorescence-guided cancer surgery and diagnosis. Nanoscale, 2017, 9: 4928–4933

46 Zheng DW, Li B, Li CX, et al. Carbon-dot-decorated carbon nitride nanoparticles for enhanced photodynamic therapy against hypoxic tumor via water splitting. ACS Nano, 2016, 10: 8715–8722

47 Zeng Q, Shao D, He X, et al. Carbon dots as a trackable drug delivery carrier for localized cancer therapy in vivo. J Mater Chem B, 2016, 4: 5119–5126

48 Feng T, Ai X, An G, et al. Charge-convertible carbon dots for

imaging-guided drug delivery with enhanced *in vivo* cancer therapeutic efficiency. ACS Nano, 2016, 10: 4410–4420

49 Ge J, Lan M, Zhou B, *et al.* A graphene quantum dot photodynamic therapy agent with high singlet oxygen generation. Nat Commun, 2014, 5: 4596

50 Ge J, Jia Q, Liu W, *et al.* Carbon dots with intrinsic theranostic properties for bioimaging, red-light-triggered photodynamic/photothermal simultaneous therapy *in vitro* and *in vivo*. Adv Healthcare Mater, 2016, 5: 665–675

51 Ge J, Jia Q, Liu W, *et al.* Red-emissive carbon dots for fluorescent, photoacoustic, and thermal theranostics in living mice. Adv Mater, 2015, 27: 4169–4177

52 Cai QY, Li J, Ge J, *et al.* A rapid fluorescence "switch-on" assay for glutathione detection by using carbon dots–MnO_2 nanocomposites. Biosens Bioelectron, 2015, 72: 31–36

53 Zhu W, Dong Z, Fu T, *et al.* Modulation of hypoxia in solid tumor microenvironment with MnO_2 nanoparticles to enhance photodynamic therapy. Adv Funct Mater, 2016, 26: 5490–5498

54 Chen Y, Ye D, Wu M, *et al.* Break-up of two-dimensional MnO_2 nanosheets promotes ultrasensitive pH-triggered theranostics of cancer. Adv Mater, 2014, 26: 7019–7026

55 Prasad P, Gordijo CR, Abbasi AZ, *et al.* Correction to multifunctional albumin–MnO_2 nanoparticles modulate solid tumor microenvironment by attenuating hypoxia, acidosis, vascular endothelial growth factor and enhance radiation response. ACS Nano, 2014, 8: 6510–6510

56 Abbasi AZ, Gordijo CR, Amini MA, *et al.* Hybrid manganese dioxide nanoparticles potentiate radiation therapy by modulating tumor hypoxia. Cancer Res, 2016, 76: 6643–6656

57 Song M, Liu T, Shi C, *et al.* Bioconjugated manganese dioxide nanoparticles enhance chemotherapy response by priming tumor-associated macrophages toward m1-like phenotype and attenuating tumor hypoxia. ACS Nano, 2016, 10: 633–647

58 Fan W, Bu W, Shen B, *et al.* Intelligent MnO_2 nanosheets anchored with upconversion nanoprobes for concurrent pH-/H_2O_2-re-

sponsive UCL imaging and oxygen-elevated synergetic therapy. Adv Mater, 2015, 27: 4155–4161

59 Yang G, Xu L, Chao Y, *et al.* Hollow MnO_2 as a tumor-micro-environment-responsive biodegradable nano-platform for combination therapy favoring antitumor immune responses. Nat Commun, 2017, 8: 902

60 Gao S, Wang G, Qin Z, *et al.* Oxygen-generating hybrid nanoparticles to enhance fluorescent/photoacoustic/ultrasound imaging guided tumor photodynamic therapy. Biomaterials, 2017, 112: 324–335

61 Fang J, Nakamura H, Maeda H. The EPR effect: unique features of tumor blood vessels for drug delivery, factors involved, and limitations and augmentation of the effect. Adv Drug Deliver Rev, 2011, 63: 136–151

62 Peng J, Dong M, Ran B, *et al.* "One-for-all"-type, biodegradable prussian blue/manganese dioxide hybrid nanocrystal for trimodal imaging-guided photothermal therapy and oxygen regulation of breast cancer. ACS Appl Mater Interfaces, 2017, 9: 13875–13886

Author contributions Wang P and Ge J supervised the project. Chen S designed and carried out the experiments, analyzed the data and wrote the manuscript. Jia Q, Zheng X and Wen Y helped with the synthesis of the CDs/MnO_2-PEG. Liu W and Zhang H helped with the photodynamic therapy.

Conflict of interest The authors declare that they have no conflict of interest.

Supplementary information Supporting data are available in the online version of the paper.

Shiqing Chen is now a Master candidate at the Technical Institute of Physics and Chemistry, Chinese Academy of Sciences. Her current research focuses on the preparation of nanomaterials for phototherapy of cancer.

Jiechao Ge is currently a full professor at the Technical Institute of Physics and Chemistry, Chinese Academy of Sciences. His research interests mainly concentrate on the synthesis of nanomaterials and their applications in phototheranostics and photocatalysts.

聚乙二醇化的碳点光敏剂/二氧化锰纳米复合物: 一种新型酸/过氧化氢响应的纳米光诊疗剂

陈诗青[1,2], 贾庆岩[1,2], 郑秀丽[1,2], 文咏梅[1,2], 刘卫敏[1,2], 张洪艳[1,2], 葛介超[1,2*], 汪鹏飞[1,2]

摘要 缺氧、过酸和过量的活性氧(如过氧化氢)是肿瘤微环境的三个主要显著特征，针对这些特征可设计酸/过氧化氢响应的诊疗剂用于增强肿瘤靶向光动力治疗效果. 本文首次利用新型碳点光敏剂还原高锰酸钾制备碳点/二氧化锰，然后利用聚乙二醇修饰形成水溶性的多功能复合物. 在正常生理环境中，该聚乙二醇化的碳点光敏剂/二氧化锰纳米复合物的荧光大部分被淬灭，光生单线态氧的能力被抑制，也不具备磁共振成像的能力. 但是在肿瘤微环境中，由于二氧化锰对酸/过氧化氢的高灵敏响应，碳点荧光恢复，同时可产生单线态氧，能够检测到强的磁共振成像信号. 因此，该水溶性聚乙二醇化的碳点/二氧化锰复合物可用于肿瘤微环境响应的荧光/磁共振双模态成像介导的光动力治疗，拓展了正电碳点作为新型光诊疗试剂在调节肿瘤微环境和增强光动力治疗方面的应用.